ISSN 1560-8034, 1605-6582 (On-line), SPQEO, 2019. V. 22, N 2. P. 237-251.

Optoelectronics and optoelectronic devices

Interaction of sub-terahertz radiation with low-doped grating-based AlGaN/GaN plasmonic structures. Time-domain spectroscopy measurements and electrodynamic modeling

V.V. Korotyeyev[1], Yu.M. Lyaschuk[1], V.A. Kochelap[1], L. Varani[2], D. Coquillat[3], S. Danylyuk[4], S. Brose[4], S.A. Vitusevich[5]

[1]*Institute of Semiconductor Physics of NAS of Ukraine, Department of Theoretical Physics, 03680 Kyiv, Ukraine*
[2]*Institute of Electronics and Systems, UMR CNRS 5214, University of Montpellier, France*
[3]*Laboratoire Charles Coulomb, UMR CNRS 5221, University of Montpellier, France*
[4]*Chair for the Technology of Optical Systems, RWTH Aachen University, 52074 Aachen, Germany Chair for the Technology of Optical Systems, RWTH Aachen University, 52074 Aachen, Germany*
[5]*Bioelectronics(ICS-8), Forschungszentrum Jülich, D-52425 Jülich, Germany*
E-mail: koroteev@ukr.net

Abstract. We have presented the results of terahertz time-domain spectroscopy measurements and a rigorous electrodynamic modeling of the optical characteristics of grating-based AlGaN/GaN plasmonic structures with low-doped two-dimensional electron gas in the frequency range of 0.1...1.5 THz. Two samples with grating aspect ratios (strip width/period) of 2.4/3 and 1.2/1.5 μm have been investigated. The measured transmission spectra are reconstructed in the calculations with high accuracy. The transmission spectra for *p*-polarized incident radiation exhibits Fabri–Pérot oscillation behavior due to the optically-thick substrate. The specific values of amplitude and spectral position of the transmission maxima are associated with the coupling of terahertz radiation with 2D electron gas due to plasmon excitations. Both calculations and transmission/reflection measurements demonstrate that plasmonic structures with micro-scaled metallic grating have three-fold increase of non-resonant absorption of terahertz radiation in comparison with the bare heterostructure. The polarization measurements of the transmission spectra of the plasmonic structures well agree with calculations and indicate a well-pronounced filtering effect of the grating for the *s*-component of the incident electromagnetic wave. The obtained values of the transmission for *p*- and *s*-polarized incident radiation demonstrate the high quality of deposited metallic grating with the extinction ratio higher than 80:1 for sub- and few THz frequency range.

Keywords: THz time-domain spectroscopy, plasmonic structure, AlGaN, metallic grating.

https://doi.org/10.15407/spqeo22.02.237
PACS 85.60.-q, 07.57-c, 42.25.Bs, 42.79.Pw

Manuscript received 16.05.19; revised version received 04.06.19; accepted for publication 19.06.19; published online 27.06.19.

1. Introduction

In the recent decade, a great success in the terahertz (THz) technologies is in part associated with the rapid development of a special field of research often mentioned as THz plasmonics [1]. From a basic scientific point of view, THz plasmonics uses the effects of strong coupling of electromagnetic (EM) waves with plasmon oscillations of electron gas in the presence of artificially structured surfaces (plasmonic metamaterials). The application area of plasmonic metamaterial-based devices involves THz-waveguiding [2], subwavelength focusing and imaging [4, 3] as well as THz emission. The latter includes plasmonic THz thermal emitters [5, 6], THz quantum cascade laser with plasmonic cavity [7] and plasmonic photoconductive switches for picosecond pulse generation [8], *etc*. The mentioned examples exploit the resonant excitation of surface plasmon-polaritons.

An important development of THz plasmonics deals with grating-based plasmonic structures coupled with a two-dimensional electron gas (2DEG) [9]. Operation principles of such hybrid plasmonic structures are based on excitation of plasmon oscillations in the conductive channel of a quantum heterostructure or in a doped sheet of graphene in the presence of a plasmonic element like

to a subwavelength metallic grating. The broad functional abilities of these structures are due to the essential wavevectror dispersion of 2DEG plasmon oscillations [10], their strong dependence on the dielectric surrounding of 2DEG [11] and small damping of the plasmons at high mobilities of 2DEG.

Moreover, these structures open the possibility to control the characteristic frequencies by the applied gate voltage [12-14] or lateral electric fields [15]. In the former case, the hybrid plasmon structure with 2DEG can be configured as a grating-gate field-effect transistor where the plasmon spectra can be modified by an applied gate-to-channel voltage leading to a spatial modulation of the 2DEG concentration. The grating-gate field-effect transistors are widely investigated as sensitive detectors of THz radiation [16-19]. In the latter case, by applying a lateral electric field, one can renormalize the plasmon spectra due to plasmonic nonreciprocity induced by Doppler effect in the presence of an electron drift. This effect can be identified as a specific splitting of the frequency band of the plasmon resonance in transmission/absorption spectra of the grating-based plasmonic structures [15, 20, 21].

Moreover, the heating effect of 2DEG by the lateral electric field can lead to the appearence of specific peaks in the emission spectra of the hybrid plasmon structure. The origin of these peaks is associated with the radiative decay of the 2D plasmons under the grating [22]. The frequency selective emission properties of the hybrid plasmon structure were recently demonstrated for highly-doped ($n_0 \sim 10^{13}$ cm^{-2}) AlGaN/GaN plasmonic structures with micron [14, 23] and submicron [24] grating periods. The above-mentioned THz thermal emitters are inherently incoherent and have broadband emissivity spectra.

The development of electrically-driven coherent THz sources remains the great challenge for modern THz technologies. The possible physical principles to develop these devices can be based on excitations of plasmon instabilities in 2DEG induced by strong steady-state electric fields. There are several mechanisms of plasmon instabilities that can be developed under the grating. One of them is Cherenkov-like instability that can be achieved when the electron drift velocity exceeds corresponding values of the phase velocity of plasmons. Theories of this type dealing with plasmon instability were proposed and discussed by K. Kempa and coworkers [25] and by S. Mikhailov [26]. At sufficiently strong applied electric fields, the conditions for the triggering of another type of convective instability associated with the effect of the stationary electric field on the high-frequency ballistic electron dynamics can be achieved. Theory of this kind of instability was recently developed in Ref. [27] using analytical solutions of the Boltzmann transport equation for an electron gas with parabolic dispersion law. It was shown that grating-based AlGaAs/GaAs plasmonic structures with deeply submicron periods at applied electric fields of the order of 1 kV/cm can possess a negative absorptivity in the THz frequency range. In the framework of similar transport models, the effects of the field induced negative absorptivity and triggering of the plasmon instability were predicted for narrow graphene strips [28] and low-doped sheet of graphene [29], respectively. Recently, another mechanism of electrically-driven plasmon instability associated with a strong renormalization of the plasmon spectra under the grating by an electron drift was proposed in Ref. [30]. This mechanism belongs to the internal type of plasmon instabilities and predicts the existence of a specific range of wavevectors within the Brillouin zone for which traveling plasmons will be unstable.

Observation and exploitation of the electron-drift-induced instabilities are possible if a set of requirements for parameters of the plasmonic structures are met. In order to decrease the threshold values of the electron drift velocities and plasmon damping due to electron scattering the plasmonic structures should use as core elements the low-doped and high-mobility quantum well heterostructures or graphene-based structures. It is also desirable to have the possibility to apply nondestructively high electric fields of the order of several kV/cm and higher to the conductive channel of the heterostructure. Finally, a large-area metallic grating of micron or sub-micron periods with small fluctuations of the strip widths and periods should be formed on the top of barrier layers.

We suggest that plasmonic structures based on low-doped AlGaN/GaN heterostructures are promising candidates to observe the above-mentioned plasmon instabilities. Moreover, low-doped AlGaN/GaN heterostructures with low collision rate for electron-electron scattering and large electron-optical phonon coupling can provide the necessary conditions to achieve the optical phonon transit-time (OPTT) resonance associated with a quasi-ballistic electron dynamics. In the past, the OPTT resonance was discussed in many papers [31-33] as an electrical mechanism for generation of EM waves in the sub- and THz frequency ranges. Later, in Ref. [34] it was shown that in the OPTT resonance regime the plasmon spectrum has a non-trivial multi-branch character that can be observed in THz spectroscopy measurements of plasmonic structures with appropriate gratings. The investigated AlGaN/GaN heterostructures [35], including the plasmonic structures [23], had electron concentrations of the order of 10^{13} cm^{-2}. However, at these high values of electron concentrations, the OPTT resonance and related phenomena are probably washed out by the strong electron-electron scattering.

The aim of this paper is to present the results of the electrodynamic modeling and THz time-domain spectroscopy (TDS) characterization of grating based AlGaN/GaN plasmonic structures with unusually low electron concentrations of the order of 10^{12} cm^{-2} achieved without any modulation doping but using the small Al content (~10%) in the barrier layer. The THz-TDS measurements were performed for large-area optical sample under equilibrium conditions. The plasmonic nature of the coupling between the electromagnetic radiation and the grating-based structures is investigated through the comparison of the electrodynamic modelling and the results of spectroscopy measurements.

The paper is organized as follows. Fabrication details, geometry and basic electric characteristics of the plasmonic structures including the details of the THz-TDS setup are highlighted in Section 2. A theoretical model and preliminary calculations are given in Section 3. The results of THz-TDS measurements their discussions and comparison with the results of the theoretical modeling are presented in Section 4. The main results are summarized in Section 5. The details of the calculations algorithms are collected in Appendix.

2. Plasmonic samples. Fabrication, basic characterization and details of THz measurements

The bare AlGaN/GaN heterostructures were grown by metal-organic vapor-phase epitaxy on a (0001) Al_2O_3 substrate with the thickness D_s = 430 μm. The resulting heterostructure consist of the undoped GaN layer followed by the $Al_{0.1}Ga_{0.3}N$ top layer with thicknesses d_1 = 3 μm and d_0 = 20 nm, respectively (see Fig. 1a). In unintentionally doped AlGaN/GaN structures, the built-in piezo- and polarization-fields form a quantum well for the electrons under the AlGaN/GaN interface. For a small Al content, the electrons are well confined near the interface, while their surface concentration, n_0, is not large. For the studied heterostructure, by performing Hall measurements, the temperature dependences of the concentration, $n_0(T_0)$, and the mobility, $\mu(T_0)$, were obtained in the wide temperature range, T_0 = 10…300 K (see Fig. 1b). The concentration of 2DEG was found to be almost constant in the considered temperature range, $\approx 2.2\cdot10^{12}$ cm^{-2}. As for the group-III-nitride structures, the electron concentration was relatively small. The latter is due to a low Al-content in the $Al_xGa_{1-x}N$ barrier layer resulting in smaller polarization doping [36]. The mobility of the electron gas was reasonably high, approximately 4500 cm^2/V·s at low temperatures (T_0 = = 10…200 K). At higher temperatures, the mobility progressively decreases down to the value 1500 cm^2/V·s at room temperature. Recently, similar AlGaN/GaN heterostructures were used as a core element for fabrication of planar GaN nanoribbons [37].

The plasmonic samples used in this study were obtained by deposition of a large-area and highly-ordered metallic grating on the top of the barrier layer. To fabrice the gold (Au) line arrays with ratios of bar width/period of 2.4 μm/3 μm (Sample 1) and 1.2 μm/1.5 μm (Sample 2), high resolution e-beam lithography (EBL) and lift-off process were used. First, the individual sample was spin-coated with the positive tone resist ZEP520A-7 diluted 4:1 in anisole, which resulted in the resist thickness close to 145 nm. Pre-exposure bake of 150 °C for 4 min was applied. Then the resist was structured by means of EBL (Vistec EBPG 5000plus tool) to create the desired line arrays. A suited exposure dose was determined using the dose test series. For this purpose, the patterned area was reduced to 250×250 μm^2, still large enough to provide a representative electron backscattering profile of the sample. Beam step size of 10 nm and beam current of 3 nA led to an optimal dose of 125 μC/cm^2 for both bar widths. The samples were developed in standard developer ZED-N50 for 90 s followed by development stop in isopropanol for 30 s and DI-rinse. For the final samples, the patterned area was enlarged to 5×5 mm^2 and the determined EBL parameters were applied. After development, the metal layer system consisting of a sticking layer of 10 nm chromium with 40 nm thick Au layer on top was deposited by electron beam evaporation setup (Pfeiffer PLS 500) with an evaporation rate of 0.1 nm/s for both metals. The lift-off was performed with the standard resist remover ZDMAC for 3 hours followed by two isopropanol baths with 30 s duration for each. For the 2.4-μm lines almost a perfect pattern over the whole grating area could be created with only three misplaced lines. For the thinner linewidth of 1.2 μm, a sticking problem was more pronounced, which resulted in peeling off approximately 5% of the lines. This effect can be effectively reduced by applying a critical point drying technique in the future studies.

The SEM images of a part of the grating coupler are shown in Fig. 1c. The area covered by the grating, S_g, was in the middle of the samples with S_g = 5×5 mm^2 for both samples. The total area of the sample, including the region without the grating, was S = 10×10 mm^2 (see sketch in Fig. 1d).

THz spectroscopy of the AlGaN/GaN plasmonic samples, including the measurements of the transmittance, reflectance and their polarization dependences, was performed using commercial THz-time-domain spectrometer TeraPulse 4000 by TeraView. The operation principles of the TeraPulse 4000 are based on the standard THz pulse technique [38]. The instrument provides generation of terahertz pulse radiation using ultra-fast (femtosecond) laser excitation of a biased GaAs photoconductive switch/antenna. The THz photoconductive antenna produces few-cycle picosecond pulses that in frequency domain cover the spectral range from 0.1 up to 3.5 THz. The power of THz radiation used for the measurements was below 1 μW, so no thermal strain was induced in the sample. Coherent detection of the terahertz radiation was performed in a similar photoconductive antenna circuit. By gating the photoconductive gap with a femtosecond pulse synchronized to THz emission, the current proportional to the terahertz electric field was measured. By varying the optical path length to the receiver, the terahertz-time domain signal was sampled.

The example of the THz pulse produced by the TeraPulse 4000 in time- and frequency-domains recorded on air is shown in Figs. 2a and 2b, respectively. The emitting THz pulse is collected and focused close to the diffraction limit. As a result a spot size on the sample is different for different Fourier harmonics (Fig. 2d).

This detail is important for a careful analysis and interpretation of the experimental data. As seen from the sketch in Fig. 2c, a large part of the sample uncovered by the grating was illuminated by radiation of lower frequencies. The higher frequency spectral components of radiation were predominantely collimated on the region

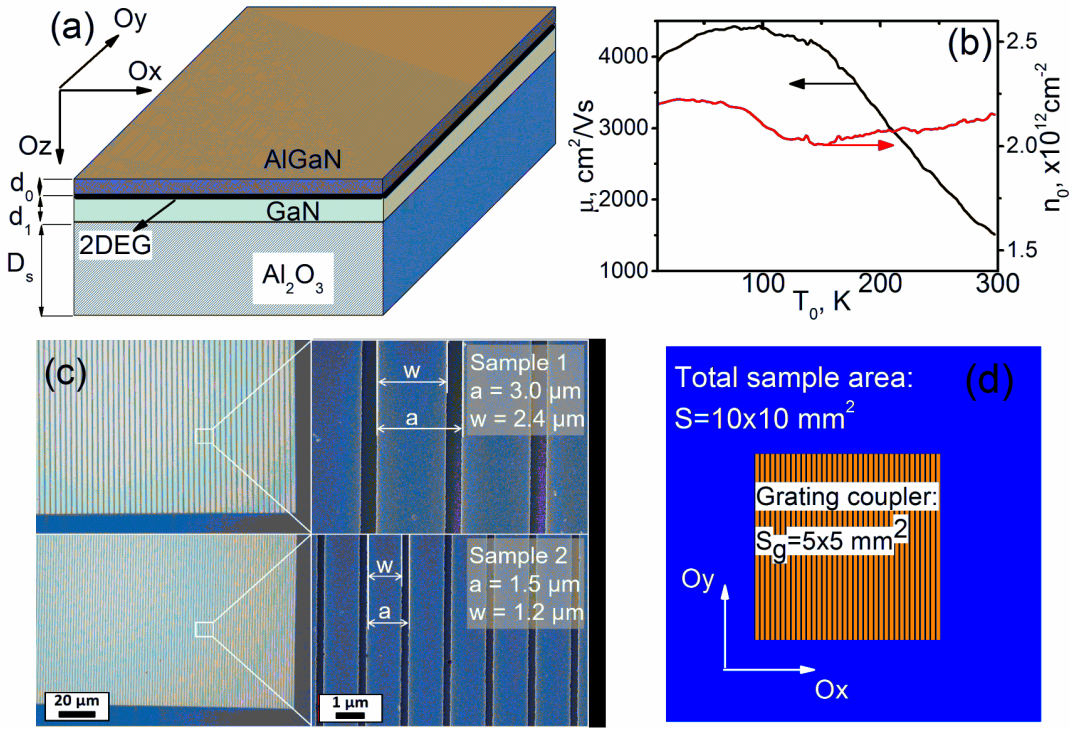

Fig. 1. (a) A schematic sketch of the bare AlGaN/GaN quantum well heterostructure. (b) Results of the measurements of temperature dependences of the mobility and the electron concentration of 2DEG. (c) Scanning electron microscopy (SEM) images of two plasmonic samples with different grating periods and strip width. (d) A sketch of the plasmonic sample with grating coupler.

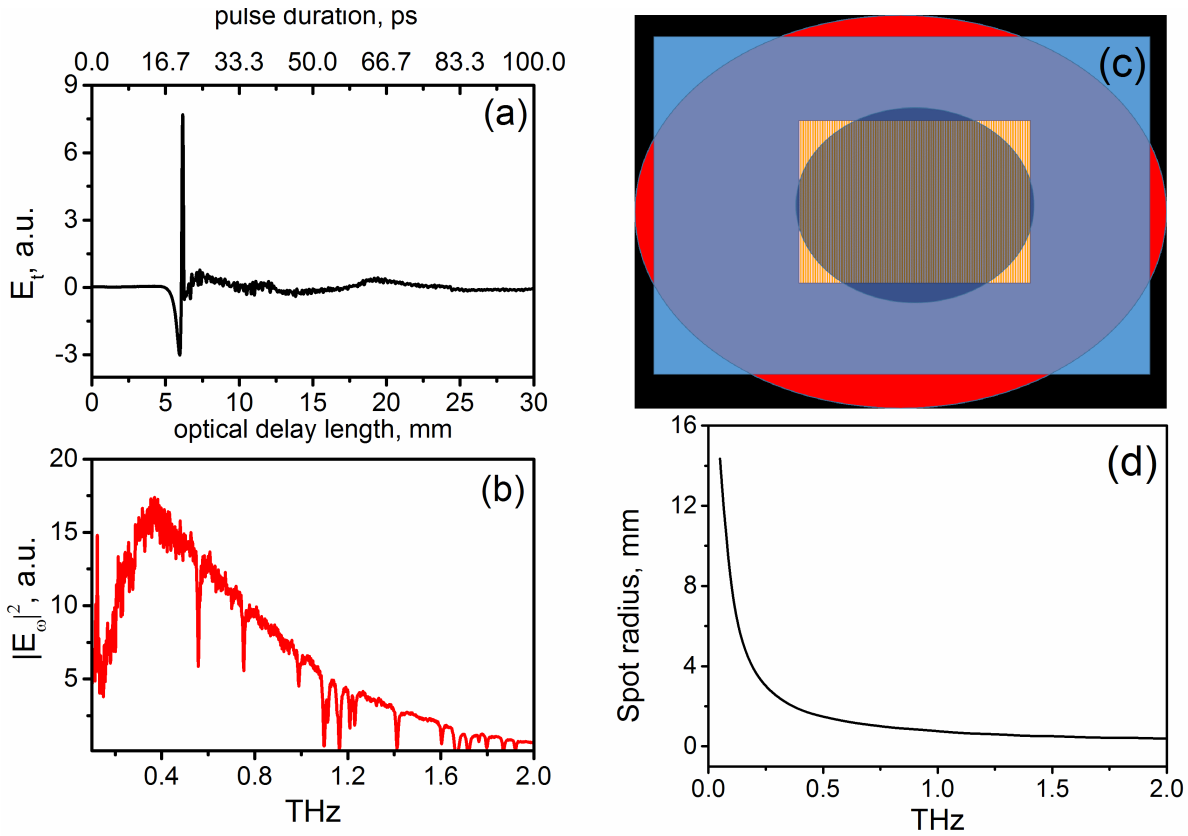

Fig. 2. (a) Waveform of the electric field of the THz pulse in the time-domain. (b) The corresponding power spectrum in the frequency-domain; (c) Sketch of the plasmonic sample illumination by different spectral harmonics. Wide red and narrow blue circles schematically illustrate the spot sizes corresponding to the lower and higher frequency harmonics, respectively. (d) Variation of the focal spot size with the frequency.

covered with the grating. The transmittance/reflectance spectrum was measured as the ratio of the power spectra of the waveform transmitted/reflected through/from the sample to the power spectrum of the reference waveform of the THz pulse. In both configurations, incoming THz radiation is linearly polarized.

3. Theoretical model and preliminary calculations

The plasmonic structures under consideration and their interaction with the THz radiation are complex and involve different electrodynamic and electronic processes. To understand expected experimental results, at first we present theoretical model describing the processes in the structures.

3.1. Theoretical model

We formulate our approach as a linear problem of interaction of the plane THz waves with the grating-based plasmonic structures. This means that the different spectral harmonics, which compose the time-domain signal, are considered as uncoupled. To analyze the electromagnetic fields, we use solutions of the Maxwell equations by applying the integral equation technique and Galerkin scheme [21, 39], which provides fast convergence and controlled accuracy of computations.

The plasmonic structure schematically shown in Fig. 1a is modeled as follows. The grating is presented as a set of infinitely thin metallic strips along the *Oy*-direction, which are periodically arranged along the *Ox*-direction (see Fig. 1d). The grating is separated by the distance d_0 from a uniform quantum well layer with electrons. The latter are considered as two-dimensional electrons situated in the $\{x, y\}$-plane. Both assumptions are valid when the thicknesses of the grating strips and the quantum well thickness are much smaller than corresponding skin-layers. Then, it is assumed that the incident THz-beam uniformly illuminates the plasmonic structures.

The master equation for the electric field, $\mathbf{E}(\mathbf{r},t)$, of the EM wave is:

$$rot\ rot\mathbf{E}(\mathbf{r},t)+\frac{\varepsilon(z)}{c^2}\frac{\partial\mathbf{E}(\mathbf{r},t)}{\partial t^2}=-\frac{4\pi}{c^2}\frac{\partial\mathbf{j}(\mathbf{r},t)}{\partial t}, \tag{1}$$

where c is the light velocity in vacuum, $\varepsilon(\mathbf{r})$ is the dielectric permittivity different for various layers composing the plasmonic structure:

$$\varepsilon(z)=\begin{cases}\varepsilon_0, & z<0,\ z>d_0+d_1+D_s,\\ \varepsilon_1, & 0<z<d_0,\\ \varepsilon_2, & d_0<z<d_0+d_1,\\ \varepsilon_3, & d_0+d_1<z<d_0+d_1+D_s.\end{cases} \tag{2}$$

Here, ε_0, ε_1, ε_2, and ε_3 stand for the dielectric permittivities of the air/vacuum, AlGaN barrier layer, GaN layer and sapphire substrate, respectively. $\mathbf{j}(\mathbf{r},t)$ is the space- and time-dependent conduction current density, which includes the currents flowing in the grating strips, $\mathbf{j}^G(\mathbf{r},t)$, and that flowing in the quantum well layer, $\mathbf{j}^{2D}(\mathbf{r},t)$.

Below, we consider the normal incidence of the plane EM wave polarized perpendicularly to the grating strips (the *p*-polarization). In this case, as the result of interaction of the incident wave with the grating, the electric field $\mathbf{E}(\mathbf{r},t)$ acquires two components, $E_x(x,z,t)$ and $E_z(x,z,t)$.

Within the proposed model, the current densities $\mathbf{j}^G$ and $\mathbf{j}^{2D}$ have only *x*-components, and the total current $\mathbf{j}$ can be written as follows:

$$j_x(\mathbf{r},t)=j_x^G(x,t)\delta(z)+j_x^{2D}(x,t)\delta(z-d_0), \tag{3}$$

where δ denotes the Dirac delta-function. To find the current in the grating, we use the Ohm law in the local approximation,

$$j^G(x,t)=\sigma^G(x)E_x(x,0,t), \tag{4}$$

where $E_x(x,0,t)$ is the *x*-component of the electric field of the THz-wave. The coordinate dependence of $\sigma^G(x)$ is determined by the grating period. In particular, for the periodic step-like grating profile, $\sigma^G(x)=\sigma^G\Theta(w-x),\ x\in[0,a]$ where Θ is the Heaviside step-function. We also assume that the conductivity of the metal strips σ^G has no frequency dispersion; this condition is realized for the majority of the highly-conductive metallic materials in the sub- and few-THz frequency range [40].

The electron current in the quantum well is described in the framework of the linear response:

$$j^{2D}(x,t)=\int_{-\infty}^{t}\sigma^{2D}(t'-t)E_x(x,d_0,t')dt', \tag{5}$$

where the Fourier component of $\sigma(t)$, *i.e.*, the frequency-dependent conductivity, can be used in the Drude–Lorentz form:

$$\sigma^{2D}(\omega)=\frac{\sigma_0}{1-i\omega\tau}. \tag{6}$$

Here, $\sigma_0=en_0\mu$ with n_0 being the electron concentration, μ is the mobility, τ – electron relaxation time, related to the electron mobility as $\tau=\mu m^*/e$; e and m^* are the elementary charge and the electron effective mass, respectively. It should be noted that the Drude–Lorentz model (6) implies dissipative high-frequency electron dynamics and neglects the effect of the spatial dispersion (wavevector-dependence) of the high-frequency conductivity. The spatial dispersion of σ^{2D} can be important for the electron gas subjected to strong stationary electric fields [26, 27].

Due to the periodicity of the plasmonic structure, we can introduce the spatial Fourier transform of the electric field and the currents with respect to the *x*-coordinate, then assuming harmonic temporal dependences with the frequency ω, we obtain:

$$\begin{bmatrix} E_{\{x,z\}}(\mathbf{r},t) \\ j_x(\mathbf{r},t) \end{bmatrix} = \sum_{m=-\infty}^{+\infty} \begin{bmatrix} E_{\{x,z\},m}(z) \\ j_{x,m}(z) \end{bmatrix} \exp\left(i[q_m x - \omega t]\right), \qquad (7)$$

where $q_m = 2\pi m/a$. Now the wave equation (1) can be transformed into a system of differential equations with respect to the *z*-coordinate (in every layer) for each *m*-spatial Fourier harmonics of the *x*-component of the electric field. For each $E_{x,m}$, we obtain:

$$\frac{d^2E_{x,m}}{dz^2} - \lambda_{r,m}^2 E_{x,m} = \frac{4\pi i \lambda_{r,m}^2}{\varepsilon_r \omega}\left[j_{x,m}^G \delta(z) + j_{x,m}^{2D}\delta(z-d_0)\right], \qquad (8)$$

where the subscripts $r = 0\ldots4$ correspond to different media: vacuum, barrier layer, buffer layer, substrate and vacuum, respectively; the characteristic parameter

$$\lambda_{r,m} = \begin{cases} \sqrt{q_m^2 - \varepsilon_r\left(\frac{\omega}{c}\right)^2}, & q_m > \sqrt{\varepsilon_r}\,\omega/c, \\ -i\sqrt{\varepsilon_r\left(\frac{\omega}{c}\right)^2 - q_m^2}, & q_m < \sqrt{\varepsilon_r}\,\omega/c \end{cases} \qquad (9)$$

describes the spatial localization of the *m*-th spatial Fourier harmonic and defines the spatial dependences of the resultant fields in the near-field zone of the grating. The *m*-th spatial Fourier harmonics of the *z*-component of the electric field $E_{z,m}$ can be expressed through $E_{x,m}$ in the following way:

$$E_{z,m} = -i\frac{q_m}{\lambda_{r,m}^2}\frac{dE_{x,m}}{dz}. \qquad (10)$$

For the case of normally-incident wave with *s*-polarization (polarization oriented along the grating strips), the electric field, $\mathbf{E}(\mathbf{r},t)$, has one non-vanishing $E_y(x, z, t)$ component. The differential equation (1) for the $E_{y,m}$-Fourier harmonics takes the form:

$$\frac{d^2E_{y,m}}{dz^2} - \lambda_{r,m}^2 E_{y,m} = -\frac{4\pi i\omega}{c^2}\left[j_{y,m}^G \delta(z) + j_{y,m}^{2D}\delta(z-d_0)\right]. \qquad (11)$$

The optical characteristics, such as the transmittance, $T_{p,s}$, and reflectance, $R_{p,s}$, are measured in the far-field zones. For the case of subwavelength grating, they are defined through the zero-order spatial Fourier harmonic:

$$T_{p,s} = \left|E_{\{x,y\},0}(d_0 + d_1 + D_s)\right|^2 \Big/ \left|\tilde{E}_0\right|^2,$$
$$R_{p,s} = \left|E_{\{x,y\},0}(0) - \tilde{E}_0\right|^2 \Big/ \left|\tilde{E}_0\right|^2, \qquad (12)$$

where $\tilde{E}_0$ is the amplitude of the incident plane wave. Having $T_{p,s}$ and $R_{p,s}$, we can calculate the absorptance of the plasmonic structure as $A_{p,s} = 1 - T_{p,s} - R_{p,s}$. The subscripts *p*, *s* denote the cases of *p*- and *s*-polarizations. The details of the mathematical procedure applied to the study of the spatial Fourier harmonics, transmittance and reflectance are given in Appendix.

3.2. Results of modeling

For the calculations, we set: the electron effective mass $m^* = 0.2m_0$, where m_0 is the free electron mass; the electron concentration $n_0 = 2\cdot10^{12}$ cm^{-2} (the same for both considered temperatures $T_0 = 77$ and 300 K). The measured electron mobility μ was equal to 4500 cm^2/V·s at $T_0 = 77$ K (the corresponding scattering time is $\tau \approx$ ≈ 0.5 ps) and 1500 cm^2/V·s at $T_0 = 300$ K (the scattering time is $\tau \approx 0.17$ ps). The dielectric permittivities of the $Al_{0.1}Ga_{0.9}N$-barrier and GaN -buffer layers are assumed to be the same, $\varepsilon_1 = \varepsilon_2 = 8.9$ corresponding to the low frequency dielectric permittivity of GaN [41]. For ε_3 of the Al_2O_3-substrate, we used the literature data [42], according to which its real part weakly changes from 9.5 up to 9.7, and its imaginary part varies from 10^{-4} to 10^{-2} in the frequency range from 0.1 up to 2 THz. The metallic grating is described by the effective two-dimensional conductivity $\sigma^G = 1.6\cdot10^{13}$ cm/s corresponding to the gold strips of thickness 40 nm at the bulk conductivity $4.0\cdot10^{17}$ s^{-1}.

The data of the spectral dependences for calculations of the transmittance and absorptance inherent to the plasmonic structures illuminated with the *p*-polarized THz wave are summarized in Figs. 3 and 4. Fig. 3 illustrates the effect on the optical characteristics related to different factors, namely: an optically-thick substrate, scales of subwavelength metallic grating and temperature. Fig. 4 enables to compare these two structures with different grating periods corresponding to Samples 1 and 2.

As seen, the substrate has a crucial impact on the transmission and absorption spectra (thin curves). The effect of the substrate is inherent for the structures with low-doped 2DEG and manifests itself as a strong modulation of the spectral characteristics with the frequency-period corresponding to the Fabry–Pérot cavity modes. The maxima and minima in the transmission/absorption spectra, respectively, are related to the positive and destructive interference of these two waves: the wave transmitted through the substrate and the wave reflected from the bottom of the substrate. This effect is common to both structures with (black lines) and without (red lines) grating coupler.

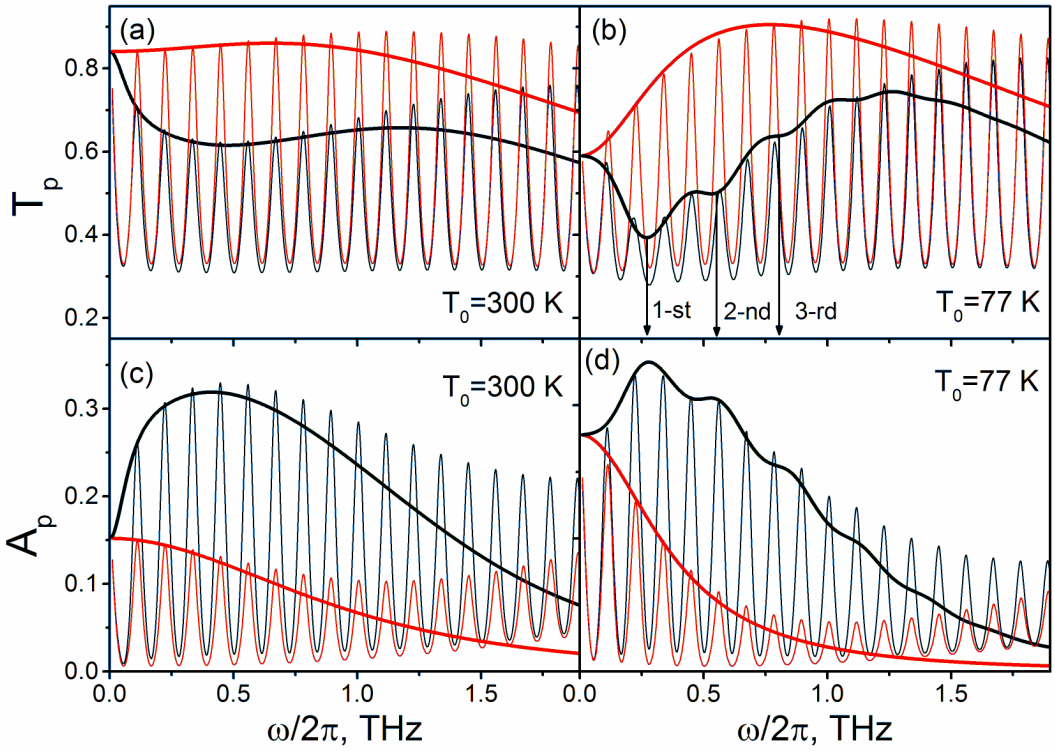

Fig. 3. Spectral dependences of the transmittance (a), (b) and the absorptance (c), (d) calculated for different temperatures. Black and red curves correspond to the sample with and without grating coupler, respectively. Thin and thick curves represent the results of calculations for the sample under test with the optically-thick substrate, $D_s \approx 430$ μm and the model sample with membrane-like structure, $D_s \approx 0$, respectively. The parameters of the grating coupler correspond to Sample 1. Other parameters of the plasmonic structure are listed in the text.

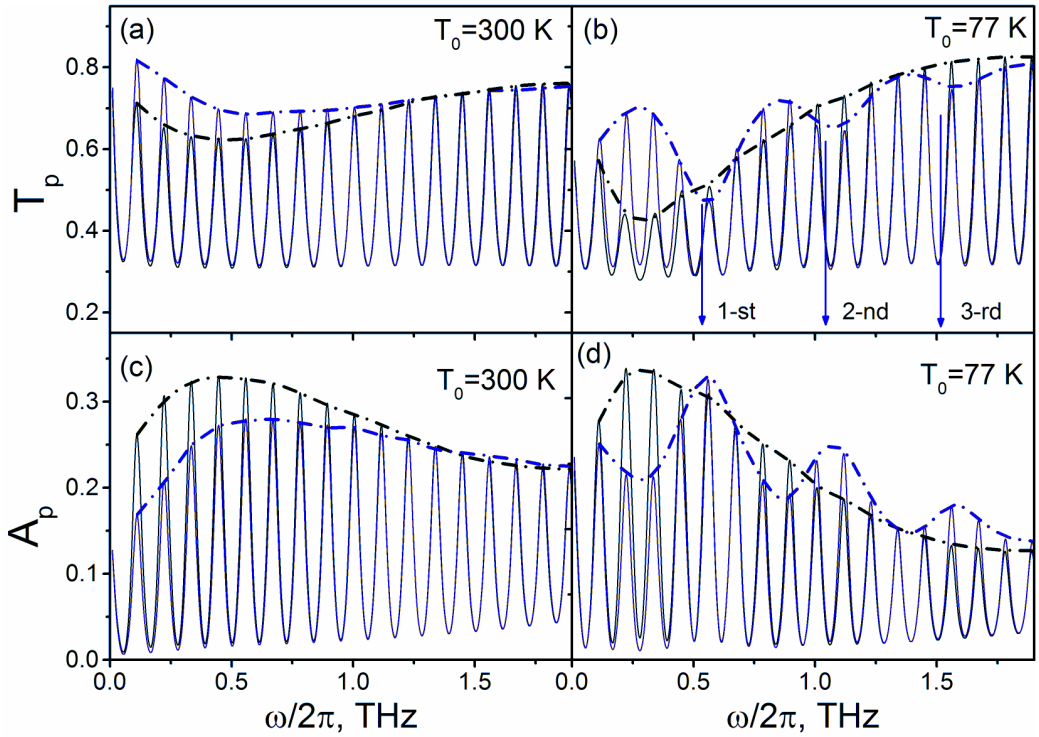

Fig. 4. Comparison of the transmittance (a), (b) and absorptance (c), (d) of Sample 1 (black curves) and Sample 2 (blue curves). Dash-dotted curves are the envelop curves of the maxima.

Let us consider structures without grating coupler. To exclude the effect of the Fabri–Pérot cavity modes, we performed the calculations for the model membrane-like structures. In this case, the obtained spectra of 80:1 and A_p (thick red curves) in the lower-frequency range (up to ≈ 0.5 THz) are represented by the envelope curves of the maxima of $T_p(\omega)$ and $A_p(\omega)$ calculated for the structures with thick substrate (red thin curves). The difference between the thick curves and the positions of the interference maxima observed in the absorption spectra (Fig. 3c) for the higher-frequency range (> 1 THz) can be explained by the dissipation effect of the THz waves in the sapphire substrate (see red thin curve in Fig. 3c). The absorption spectra of the membrane-like structure (red thick curves in Figs. 3c and 3d) have monotonic, Lorentz-type behavior. This behavior corresponds to the spectral dependence of the real part of the dynamic conductivity of 2DEG,

$$Re\left[\sigma^{2D}\right] = \frac{\sigma_0}{1+\omega^2\tau^2}.$$

According to this expression, we obtain a larger absorption of sub-THz radiation (0…0.3 THz) at lower temperatures and larger absorption of THz radiation (1…2 THz) at higher temperatures (compare these two red thick curves in Figs. 3c and 3d). For example, the absorptance at 1 THz of the membrane-like structure uncovered with the grating is equal to 7% and 4% at T_0 = 300 K and T_0 = 77 K, respectively.

As seen (black curves in Fig. 3), the use of the grating coupler on the top of the barrier layer essentially increases the capability of the structure in absorption of THz radiation. This capability is related to the near-field effects, *i.e*., a significant concentration of the energy of the THz wave under the grating and, particularly, in the quantum well with 2DEG. Even at room temperature (panels (a) and (c)) the transmission of THz waves through the plasmonic structure is strongly suppressed within the frequency range 0.1…1.5 THz, which is accompanied by the three-fold increase in absorption as compared to the bare heterostructure. The plasmonic structures show well-pronounced non-monotonic behavior of the transmittance and absorptance. The appearance of frequency maximum in the absorptance (frequency minimum in the transmittance) is related to excitations of plasmon modes in 2DEG under the grating.

The plasmon resonance frequencies can be estimated using the dispersion law of the gated plasmons obtained for double-layered structure in the electrostatic approximation [11, 21]

$$\omega_m = \sqrt{\frac{4\pi e^2 n^{2D}|q_m|}{m^* \varepsilon_{eff}(q_m)}}, \qquad (13)$$

where $\varepsilon_{eff}(q_m)$ is the effective dielectric permittivity given by the following expression:

$$\varepsilon_{eff}(q_m) = \varepsilon_1 \mathrm{cth}\left(|q_m| d_0\right) + \varepsilon_2 \frac{\varepsilon_0 + \varepsilon_2 \mathrm{cth}|q_m| d_1}{\varepsilon_2 + \varepsilon_0 \mathrm{cth}|q_m| d_1}.$$

The estimations give that the first three resonance frequencies are $\omega_{1,2,3}$ = 0.27, 0.54, 0.79 THz for the grating period, a = 3 μm and $\omega_{1,2,3}$ = 0.54, 1.03, 1.49 THz for the grating period, a = 1.5 μm.

At room temperature, the effect of the plasmon resonances is strongly broadened due to the short electron relaxation time. However, the calculations predict well-pronounced plasmon resonances (see black curves in Fig. 3b and 3d) at liquid nitrogen temperatures. These resonances manifest itself as characteristic dips in the transmission spectra of the membrane-like plasmonic structure and as a non-monotonic behavior of the Fabri–Pérot maxima for the case of thick substrates. The resonance frequencies ω_m calculated according to Eq. (13) are shown by arrows in Figs. 3b and 4b. As seen, the values of the plasma frequencies ω_m almost correspond to the positions of characteristic dips in low-temperature transmission spectra. This good agreement between the results of the rigorous electrodynamic modeling and the approximate expression (13) occurs for the grating with large filling factor, *w*/*a* close to 1. This factor is equal to 0.8 for both samples under test.

Fig. 4 provides the comparison of these two plasmonic structures with different grating periods. At room temperature, the transmission/absorption spectra of these two structures are similar. However, a shift of the minimum/maximum of the envelope curves to the higher frequency range can be seen for the sample with smaller *a* (blue curves). The larger difference should be observed at T_0 = 77 K. For the sample with smaller *a*, the plasmon resonances are shifted to the higher-frequency range and they become more pronounced.

4. Experimental results, their analysis and discussions

Modification of the form of THz pulse as a result of the passage through the plasmonic structure is shown in Fig. 5a. As seen, the amplitudes and the position in time of the main peak in the time-domain signal transmitted through the sample (red curve) is decreased and shifted in comparison with the reference signal. The decrease of the amplitude can be attributed to energy losses of the THz pulse due to absorption in the plasmonic structure and partial reflection from the interfaces. The delay time of the main peak is related to deceleration in the optically dense substrate. The effect of the substrate can be also identified as the appearance of additional and much lower peaks, which are echos of the main peak. The time interval between the main peak and the first echo corresponds to the time of double pass of the pulse through the substrate.

The appearance of these echos in the time domain produces characteristic oscillations of the spectral (Fourier) components of the transmitted signal (see red curve in the inset to Fig. 5a). In the frequency domain, the period of these oscillations corresponds to the period

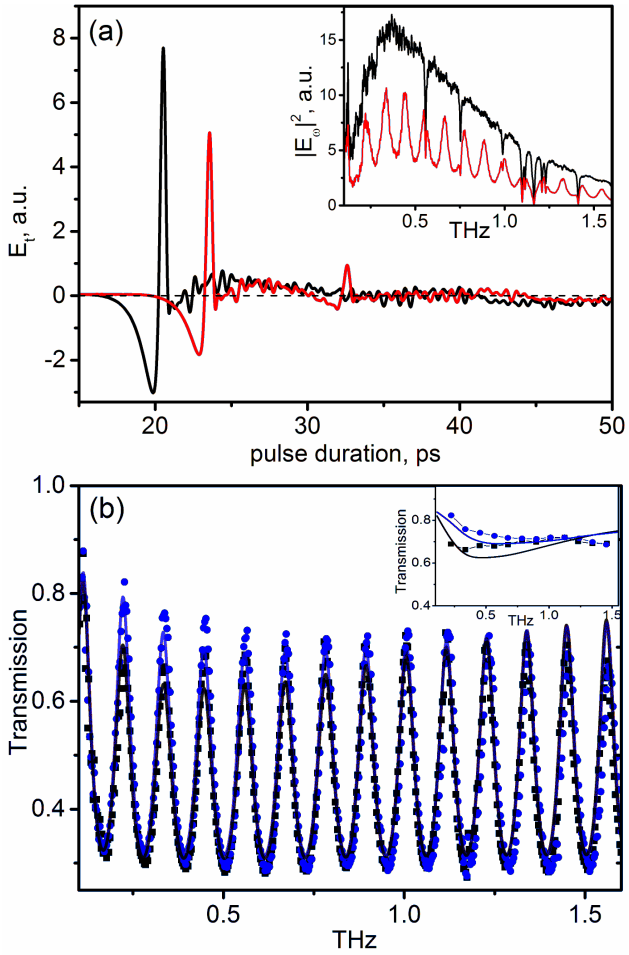

Fig. 5. (a) The reference (black) and transmitted through the Sample 1 (red) signals. In the inset: corresponding power spectra of these signals. (b) Thin solid curves are calculated transmission spectra, $T_{tot}(\omega)$ for Sample 1 (black curve) and Sample 2 (blue curve). Dotted curves are measured transmission spectra for Sample 1 (black squires) and Sample 2 (blue circles). In the inset: corresponding envelope curves. The polarization angle, $\alpha = 0$ is the same for both measurements.

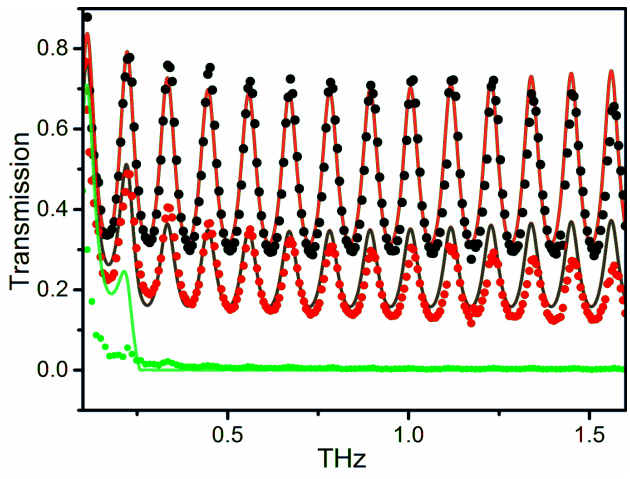

Fig. 6. Transmission spectra of Sample 2 for different polarization angles, $\alpha = 0°$, 45°, and 90° (black, red and green curves, respectively). Solid lines are the results of calculations according to Eq. (14). Circles are the results of the measurements.

of Fabri–Pérot cavity modes. The measured transmission spectrum is the ratio of the squared Fourier component, $|E_\omega|^2$, of the transmitted and reference pulses. The obtained room-temperature transmission spectra for the Samples 1 and 2 are shown in Fig. 5b by black and blue dots, respectively.

In our experiments, the incident THz pulses illuminated the samples completely, including the part covered with the grating and the uncovered one (see Fig. 1d). Moreover, as discussed above, the focal spot of illumination was dependent on the frequency (see Figs. 2c and 2d). These factors should be taken into account when comparing the experimental results with the modeling ones and drawing conclusions on the coupling of the plasmonic structures with the THz radiation. In the following equations for the calculated transmission T_{tot} and reflection R_{tot} spectra, we took into account the above mentioned factors, as well as different polarization angles α with respect to the grating orientation:

$$T_{tot}(\omega) = \left[\begin{array}{l}\left(T_p(\omega)\cos(\alpha)^2 + T_s(\omega)\sin(\alpha)^2\right)S_g + \\ + T_h(\omega)\left(S_{sp}(\omega) - S_g\right)\end{array}\right] \Big/ S_{sp}(\omega),$$

if $S_{sp} > S_g$,

$$T_{tot}(\omega) = T_p(\omega)\cos(\alpha)^2 + T_s(\omega)\sin(\alpha)^2, \text{ if } S_{sp} < S_g. \qquad (14)$$

Here, T_p and T_s are the transmittances obtained for spatially-unrestricted plasmonic structure for *p*- and *s*-polarization ($\alpha = 0°$ and $\alpha = 90°$, respectively) of the incident EM wave. T_h is the transmittance of the bare heterostructure. The latter can be calculated in the framework of the discussed algorithms by setting $\sigma^G = 0$. Eq. (14) can be applied if the spot area $S_{sp}(\omega)$ is smaller than the sample surface S. The frequency dependent $S_{sp}(\omega)$ can be estimated as $S_{sp}(\omega) = \pi r_{sp}^2(\omega)$, where the spot radius, $r_{sp}(\omega)$, is presented in Fig. 2d. After substitution of $T_{p,s,h} \to R_{p,s,h}$, the same equation (14) can be used for the calculation of the reflection spectra.

The results of calculations of $T_{tot}(\omega)$ are presented in Fig. 5b. Comparing these results with the measurements presented in the same figure, one can see that the measured transmission spectra of both samples are well-described by the proposed model. Within small experimental errors, the calculations reproduce all peculiarities of the measured curves such as, for example, the increase of the transmission maximum in the low-frequency range, $\omega/2\pi \approx 0.1$ THz. We remark that, at this frequency, the spot area is so large that a considerable part of the surface uncovered by the grating is illuminated (see Fig. 2c). In the higher frequency range, when the spectral components of the THz pulse are collimated on the grating, the transmission maxima are decreased as a result of the enhanced coupling between THz radiation and 2DEG. The envelope curves

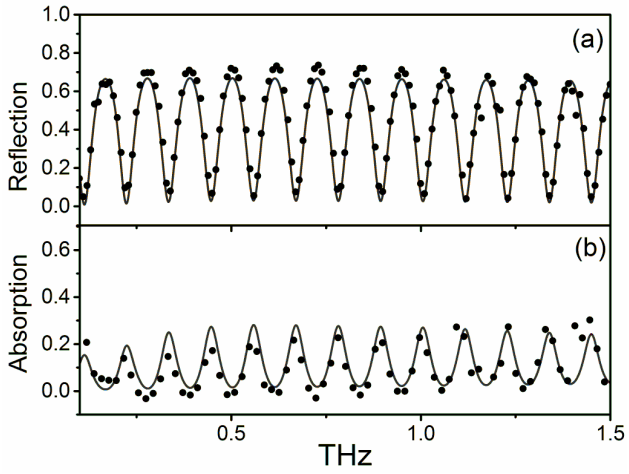

Fig. 7. Reflection (a) and absorption (b) spectra of Sample 2 for *p*-polarization. Solid lines are the results of calculations. Circles correspond to the measurements. Calculated absorption spectrum of the bare heterostructure is shown with the dash-dotted line.

of the maxima of the measured transmission spectra for both samples are in good agreement with calculations, and their behavior emphasizes the plasmonic nature of the coupling of THz radiation with 2DEG.

The measured polarization dependences of the transmission spectra are presented in Fig. 6 for Sample 2. As seen, the obtained results of the transmission measurements practically coincide with the calculations at different angles of the polarization, $\alpha = 0°$, 45°, 90°, in the wide frequency range 0.1 to 1 THz.

Due to the filtering effect of the grating for the electric field component corresponding to *s*-polarization, the transmission essentially decreases at $\alpha = 45°$, as well as the amplitudes of the Fabri–Pérot oscillations. At $\alpha = 90°$ (*s*-polarization) the transmission is almost totally suppressed: indeed, the observable values of transmission are less than 1%. Comparing this value with the maximum of the transmission obtained for the case of *p*-polarization, we can conclude that the extinction ratio of the grating-based plasmonic structures is 80:1 for the sub- and THz frequency ranges: it confirms the high quality of the fabricated grating coupler.

The measurement of the reflection spectra facilitates determination of the absorptance for the plasmonic structures. In Fig. 7a, the measured and calculated reflection spectra are shown for *p*-polarized illumination (Sample 2), while the corresponding absorptance is presented in Fig. 7b. One can see the good agreement between experimental and theoretical data in the whole analyzed frequency range.

The obtained results indicate a significant enhancement of interaction for sub- and THz radiation with 2DEG assisted by the metallic grating couplers. For example, at the frequency equal to 1 THz the grating provides the maximum absorption value 27%, which is three times higher than that for the bare AlGaN/GaN heterostructure (see dash-dotted curve in Fig. 7b).

5. Conclusions

We have performed a comprehensive analysis of the optical characteristics of grating-based low-doped AlGaN/GaN plasmonic structures within the frequency range 0.1 to 1.5 THz. The fabrication process of the plasmonic sample, THz time-domain spectroscopy measurements and approaches used for the theoretical modeling have been discussed in details. The room temperature measurements indicate a significant grating-assisted enhancement of the coupling of sub-THz electromagnetic waves with 2DEG. This coupling is associated with the non-resonant excitations of plasmon modes in the 2DEG channel. The plasmonic nature of this effect was identified as a characteristic shift of the envelope curve of the transmission maxima for the sample with smaller grating period. We found that, due to the substrate, a strong modulation of the transmission/reflection spectra by the Fabri–Perot resonances takes place for AlGaN/GaN plasmonic structure with the low electron concentrations $1…2\cdot10^{12}$ cm^{-2}. The existence of this modulation can negatively affect observation of plasmon resonances. For further investigations of the THz properties of such plasmonic structures in the external electric fields, the samples should be provided by antireflection coatings at the bottom interface or samples with membrane-like substrates can be used. The polarization measurements of the transmission spectra revealed the high quality of the deposited metallic grating with an extinction ratio higher than 80:1 for the sub-THz frequency range.

The theoretical modeling of grating based plasmonic structure was based on the rigorous solution of Maxwell's equations using the Fourier expansion of the electric field components of EM waves in the coordinate space and the integral equation technique. The calculation algorithm was developed for the multi-layered geometry of the samples and for *p*- and *s*-polarized normally incident plane EM wave. In contrast to commercial software that typically uses the finite-element schemes, the proposed method gives a fast convergence and can be applied for the calculations of the optical characteristics for plasmonic structures with deeply subwavelength elements. The results of the modeling and measurements at room temperature were in a good agreement. The modeling predicts further enhancement of THz waves-plasmonic structure coupling with decreasing the temperatures.

The presented results and, in particular, the enhanced coupling of the THz waves with high-mobility low-dimensional electrons allow us to suggest that the plasmonic structures based on low-doped AlGaN/GaN heterostructures are the well-promising candidate for observation of the plasmon instabilities mentioned in Introduction. Indeed, the AlGaN/GaN heterostructures with low electron concentrations ($n_0 \le 10^{12}$ cm^{-2}) demonstrate plasmonic oscillations with the frequencies 1 THz at the wavevectors of the order of 10^5 cm^{-1}, which can be efficiently excited in plasmonic structures with grating periods ≤1 μm. Due to the peculiar character of

the electron-optical phonon interaction in these structures [34], the plasmonic instability can be induced in moderate stationary electric fields (1…5 kV/cm).

6. Appendix

Looking for the solution of Eq. (8) in the form of a superposition of transmitted and reflected waves in each layer and using the appropriate boundary conditions at the *r*-th interface:

$$E_{x,m}\,|_{z=z_r+0} = E_{x,m}\,|_{z=z_r-0}, \tag{15}$$

$$\frac{\varepsilon_r}{\lambda_{r,m}^2}\frac{dE_{x,m}}{dz}\bigg|_{z=z_r+0} - \frac{\varepsilon_{r-1}}{\lambda_{r-1,m}^2}\frac{dE_{x,m}}{dz}\bigg|_{z=z_r-0} =$$

$$= \frac{4\pi i}{\omega}\left[j_{x,m}^{G}\delta_{r,1} + j_{x,m}^{2D}\delta_{r,2}\right] \tag{16}$$

together with Eqs. (4) and (5) written in the Fourier representations, $j_{x,m}^{G} = \sum_m \sigma_{m-m'}^{G} E_{x,m'}(0)$, $j_{x,m}^{2D} = \sigma_m^{2D} E_{x,m}(d_0)$, we can obtain the infinite system of algebraic equations formulated for the spatial *m*-th Fourier harmonics of the electric field in the grating plane:

$$\sum_{m'}\left[\delta_{m,m'} + \frac{2\pi i\lambda_{0,m}W_{p,m}}{\varepsilon_0\omega}\sigma_{m-m'}^{G}\right]E_{x,m'}(0) = W_{p,m}\delta_{m,0}\tilde{E}_0 . \tag{17}$$

The coupling factor, $W_{p,m}$, for the case of *p*-polarized incident wave includes all geometrical and high-frequency parameters of the layers as well as 2DEG. The cumbersome analytical expression of this factor for the structure "grating – barrier layer – 2DEG – substrate" is given in Ref. [21].

If the plasmonic structure has a more complicated geometry (see sketch in Fig. 8) with *N* interfaces that separate the different $N + 1$ media, $W_{p,m}$ can be expressed as follows:

$$W_{p,m} = \frac{2}{1+\beta_{1,m}\left[1-R_{1,m}\right]/\left[1+R_{1,m}\right]}, \tag{18}$$

where $\beta_{r,m} = \varepsilon_r\lambda_{r-1,m}/\varepsilon_{r-1}\lambda_{r,m}$ and $R_{r,m} \equiv A_{r,m}/B_{r,m}\exp(2\lambda_{r,m}z_r)$ is the ratio of reflective and transmitted waves in the *r*-th layer ($r = 1…N$). The value of $R_{1,m}$ for each *m*-th Fourier harmonic can be obtained iteratively, using the following recursive relationship [43].

$$R_{r-1,m} = \frac{(1+R_{r,m})\Lambda_{r,m}^{-} - (1-R_{r,m})\beta_{r,m}}{(1+R_{r,m})\Lambda_{r,m}^{+} + (1-R_{r,m})\beta_{r,m}}\times$$

$$\times\exp[2\lambda_{r-1,m}(z_{r-1}-z_r)],\ r = N..2. \tag{19}$$

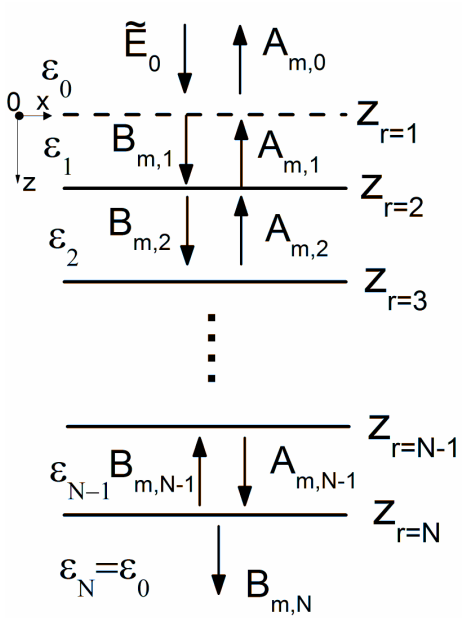

Fig. 8. Sketch of the geometry of multilayered plasmonic structure.

Starting from $R_{N,m} = 0$ and applying the iterative procedure $N - 1$ times, we can numerically calculate $R_{1,m}$. The condition $R_{N,m} = 0$ denotes the absence of the reflected waves under the lowest interface of the structure. Eq. (19) is obtained under assumption of possible existence of 2DEG with σ_r^{2D} at the *r*-th interface (for our structure $\sigma_{r,m}^{2D} = \sigma_m^{2D}\delta_{2,r}$). The parameters $\Lambda_{r,m}^{\pm} = 1 \pm 4\pi i\sigma_{r,m}^{2D}\lambda_{r-1}/\omega\varepsilon_{r-1}$ take it into account.

Having $E_{x,m}(0)$, the reflectivity R_p is straightforwardly given by

$$R_p = \left|E_{x,0}(0)/\tilde{E}_0 - 1\right|^2. \tag{20}$$

The transmitivity can be obtained as

$$T_p = \left|T_{N,0}/\tilde{E}_0\right|^2. \tag{21}$$

Calculation of $T_{N,0}$ requires the use of the following recursive formula:

$$T_{r+1} = T_r\frac{1+R_r\exp\left(2\lambda_{r,m}[z_{r+1}-z_r]\right)}{1+R_{r+1}}\times$$

$$\times\exp\left(-\lambda_{r,m}[z_{r+1}-z_r]\right),\ r = 1..N-1, \tag{22}$$

where the starting value T_1 can be calculated as $T_1 = E_{x,m}(0)/\left(1+R_{1,m}\right)$.

It should be noted that the solutions of Eqs. (17) have slow convergence with respect to the rank of the system. Therefore, usage of the direct Fourier method for

the case of *p*-polarization is ineffective from the viewpoint of computational time. This difficulty can be overcome using the method of integral equations. For this purpose, the system (17) can be rewritten in the coordinate representation in the form of a linear integral equation with respect to spatial distribution of the *x*-component of the electric field in the grating plane:

$$E_x(x,0) = W_0\tilde{E}_0 - \int_{-w/2}^{w/2} dx' L(x,x') E_x(x',0), \quad (23)$$

where $L(x,x')$ is the kernel of the integral operator:

$$L(x,x') = \frac{2\pi i}{\varepsilon_0 \omega} \frac{\sigma^G(x')}{a} \sum_m \lambda_{0,m} W_{p,m} e^{iq_m(x-x')}. \quad (24)$$

The Galerkin scheme can be used for the solution of Eq. (23) with the expansion of the electric field distribution in the strips in terms of orthogonal polynomials, $\{O_l\}$, $l = 0..\infty$. For the step-like profile of the grating conductivity assumed in the calculations, the Legendre polynomials are used as a basis. Substituting the expansion of the field $E_x(\tilde{x},0) = \sum_{l=0}^{M_l} C_l O_l(\tilde{x})$ ($\tilde{x} = 2x/w$, $|\tilde{x}| \le 1$), Eq. (23) transforms into a system of algebraic equations with respect to the expansion coefficients C_l:

$$\sum_{l'=0}^{M_l} G_{l,l'} C_{l'} = W_0 \tilde{E}_0 \delta_{l,0}, \quad (25)$$

where

$$G_{l,l'} = \frac{2}{2l+1}\delta_{l,l'} + \frac{i\pi f \sigma^G}{\omega \varepsilon_0} \sum_m \lambda_{0,m} W_m \zeta_{l,m} \zeta^*_{l',m} \quad (26)$$

with the grating filling factor $f = w/a$ and

$$\zeta_{l,m} = \int_{-1}^{1} O_l(\tilde{x}) e^{i\pi m f \tilde{x}} d\tilde{x}.$$

By finding the coefficients C_l, we can express the Fourier-harmonics of the field in the grating plane:

$$E_{x,m}(0) = W_0\tilde{E}_0\delta_{m,0} - \frac{i\pi f\sigma^G}{\omega\varepsilon_0}\lambda_{0,m}W_{p,m}\sum_l C_l\zeta^*_{l,m} \quad (27)$$

thus allowing to calculate the reflectivity R_p and the transmittivity T_p according to Eqs. (20) and (21), respectively.

The projection of the integral equation (23) on the Legendre polynomials results in the fast convergent matrix equation (25). Indeed, the use of $M_l = 10$ polynomials provides the computational accuracy of the spectral characteristics higher than 0.1%.

For the case of *s*-polarized normally incident EM wave, the boundary conditions used for the solution of Eq. (11) are as follows

$$E_{y,m}\Big|_{z=z_r+0} = E_{y,m}\Big|_{z=z_r-0}, \quad (28)$$

$$\frac{dE_{y,m}}{dz}\Big|_{z=z_r-0} - \frac{dE_{y,m}}{dz}\Big|_{z=z_r+0} = \frac{4\pi i\omega}{c^2}\left[j^G_{y,m}\delta_{r,1} + j^{2D}_{y,m}\delta_{r,2}\right]. \quad (29)$$

The transmission and reflection spectra can be directly obtained using the solution of the system of Eqs. (30):

$$\sum_{m'}\left[\delta_{m,m'} - \frac{2\pi i\omega W_{s,m}}{c^2\lambda_{0,m}}\sigma^G_{m-m'}\right]E_{y,m'}(0) = W_{s,m}\delta_{m,0}\tilde{E}_0, \quad (30)$$

where

$$W_{s,m} = \frac{2}{1+\lambda_{1,m}\left[1-R_{1,m}\right]/\lambda_{0,m}\left[1+R_{1,m}\right]}. \quad (31)$$

The recursive relationship of Eq. (19) takes the form

$$R_{r-1,m} = \frac{\left(1+R_{r,m}\right)\Lambda^+_{r,m} - \left(1-R_{r,m}\right)\lambda_{r,m}/\lambda_{r-1,m}}{\left(1+R_{r,m}\right)\Lambda^-_{r,m} + \left(1-R_{r,m}\right)\lambda_{r,m}/\lambda_{r-1,m}} \times \exp\left[2\lambda_{r-1,m}\left(z_{r-1}-z_r\right)\right] \quad (32)$$

with $\Lambda^{\pm}_{r,m} = 1 \pm 4\pi\omega i\sigma^{2D}_{r,m}/c^2\lambda_{r-1,m}$. For the calculations of the transmission spectra, Eq. (22) should be used with $T_1 = E_{y,m}(0)/\left(1+R_{1,m}\right)$ and $R_{r,m}$ that are given by the relationship (32).

Acknowledgments

This work is supported by the Ministry of Education and Science of Ukraine (Project M/24-2018), by the German Federal Ministry of Education and Research (BMBF Project 01DK17028), by the Occitanie region via the Gepeto Terahertz platform and by the Doctoral Training Network in Terahertz Technologies for Imaging, Radar and Communication Applications, TeraApps (H2020-MSCA-ITN-2017, grant number 765426).

References

1. Rahm M., Nahata A., Akalin T., Beruete M. and Sorolla M. Focus on terahertz plasmonics. *New J. Phys.* 2015. **17**. P. 100201; https://doi.org/10.1038/nphoton.2013.235.
2. Zhang Y., Xu Y., Tian C. et al. Terahertz spoof surface-plasmon-polariton subwavelength waveguide. *Photonics Research.* 2018. **6**. P. 18; https://doi.org/10.1364/PRJ.6.000018.

3. Kawano Y. and Ishibashi K. On-chip near-field terahertz detection based on a two-dimensional electron gas. *Physica E*. 2010. **42**. P. 1188–1191; https://doi.org/10.1016/j.physe.2009.11.082.
4. Serita K., Mizuno S., Murakami H., Kawayama I., Takahashi Y., Yoshimura M., Mori Y., Darmo J., and Tonouchi M. Scanning laser terahertz near-field imaging system. *Opt. Exp.* 2012. **20**. P. 12959–12965; https://doi.org/10.1364/OE.20.012959.
5. Kang C., Leem J.W., Maeng I., Kim T.H., Lee J.S., Yu J.S., and Kee C.-S. Strong emission of terahertz radiation from nanostructured Ge surfaces. *Appl. Phys. Lett.* 2015. **106**. P. 261106; https://doi.org/10.1063/1.4923372.
6. Melentev G.A., Shalygin V.A., Vorobjev L.E. et al. Interaction of surface plasmon polaritons in heavily doped GaN microstructures with terahertz radiation. *J. Appl. Phys.* 2016. **119**. P. 093104; https://doi.org/10.1063/1.4943063.
7. Saliha M., Dean P., Valavanis A., Khanna S.P., Li L.H., Cunningham J.E., Davies A.G., and Linfield E.H. Terahertz quantum cascade lasers with thin resonant-phonon depopulation active regions and surface-plasmon waveguides. *J. Appl. Phys.* 2013. **113**. P. 113110; https://doi.org/10.1063/1.4795606.
8. Berry C.W. and Jarrahi M. Terahertz generation using plasmonic photoconductive gratings. *New J. Phys.* 2012. **14**. P. 105029; https://doi.org/10.1088/1367-2630/14/10/105029.
9. Otsuji T. and Shur M. Terahertz Plasmonics: Good Results and Great Expectations. *IEEE Microwave Magazine.* 2014. **15**. P. 43–50; https://doi.org/10.1109/MMM.2014.2355712.
10. Chaplik A.V. Absorption and emission of electromagnetic waves by two-dimensional plasmons. *Surf. Sci. Rep.* 1985. **5.** P. 289; https://doi.org/10.1016/0167-5729(85)90010-X.
11. Popov V.V. Plasmon excitation and plasmonic detection of terahertz radiation in the grating-gate field-effect-transistor structures. *J. Infrared, Millimeter, Terahertz Waves.* 2011. **32**. P. 1178–1191; https://doi.org/10.1007/s10762-011-9813-6.
12. Popov V.V., Polischuk O.V., Teperik T.V., Peralta X.G., Allen S.J., Horing N.J.M., Wanke M.C. Absorption of terahertz radiation by plasmon modes in a grid-gated double-quantum-well field-effect transistor. *J. Appl. Phys.* 2003. **94**. P. 3556; https://doi.org/10.1063/1.1599051.
13. Dyer G.C., Aizin G.R., Preu S., Vinh N.Q., Allen S.J., Reno J.L. and Shaner E.A. Inducing an incipient terahertz finite plasmonic crystal in coupled two dimensional plasmonic cavities. *PRL.* 2012. **109**. P. 126803; https://doi.org/10.1103/PhysRevLett.109.126803.
14. Qin H., Yu Y., Li X., Sun J., Huang Y. Excitation of terahertz plasmon in two-dimensional electron gas. *Terahertz Sci. and Technol.* 2016. **9**. P. 71; https://doi.org/ 10.11906/TST.71-81.2016.06.07.
15. Bhatti A.S., Richards D., Hughes H.P., Ritchie D.A. Spatially resolved Raman scattering from hot acoustic and optic plasmons. *Phys. Rev. B.* 1996. **53**. P. 11 016; https://doi.org/10.1103/PhysRevB.53.11016.
16. Popov V.V., Fateev D.V., Otsuji T., Meziani Y.M., Coquillat D., Knap W. Plasmonic terahertz detection by a double-grating-gate field-effect transistor structure with an asymmetric unit cell. *Appl. Phys. Lett.* 2011. **99.** P. 243504; https://doi.org/10.1063/1.3670321.
17. Watanabe T., Boubanga-Tombet S., Tanimoto Y. et al. Ultrahigh sensitive plasmonic terahertz detector based on an asymmetric dual-grating gate HEMT structure. *Solid-State Electronics.* 2012. **78**. P. 109–114; https://doi.org/10.1016/j.sse.2012.05.047.
18. Yermolayev D.M., Maremyanin K.M., Fateev D.V. et al. Terahertz detection in a slit-grating-gate field-effect-transistor structure. *Solid-State Electronics.* 2013. **86**. P. 64–67; https://doi.org/10.1016/j.sse.2012.09.009.
19. Olbrich P., Kamann J., Konig M. et al. Terahertz ratchet effects in graphene with a lateral superlattice. *Phys. Rev. B.* 2016. **93**. P. 075422; https://doi.org/10.1103/PhysRevB.93.075422.
20. Borgnia Dan S., Phan Trung V., Levitov L.S. Quasi-relativistic doppler effect and non-reciprocal plasmons in graphene. *ArXiv:1512.09044* (2015).
21. Lyaschuk Yu.M. and Korotyeyev V.V. Theory of detection of terahertz radiation in hybrid plasmonic structures with drifting electron gas. *Ukr. J. Phys.* 2017. **62**. P. 889; https://doi.org/10.15407/ujpe62.10.0889.
22. Krasheninnikov M.V. and Chaplik A.V. Radiative decay of two-dimensional plasmons. *Zh. Eksp. Teor. Fiz.* 1985. **88**. P. 129–133.
23. Jaktas V., Grigelionis I., Janonis V. et al. Electrically driven terahertz radiation of 2DEG plasmons in AlGaN/GaN structures at 110 K temperature. *Appl. Phys. Lett.* 2017. **110**. P. 202101; https://doi.org/10.1063/1.4983286.
24. Zheng Zhongxin, Sun Jiandong, Zhou Yu, Zhang Zhipeng, Qin Hua, Broadband terahertz radiation from a biased two-dimensional electron gas in an AlGaN/GaN heterostructure. *J. Semicond.* 2015. **36**. P. 104002; https://doi.org/10.1088/1674-4926/36/10/104002.
25. Kempa K., Bakshi P., Xie H., Schaich W.L. Current-driven plasma instabilities in solid-state layered systems with a grating. *Phys. Rev. B.* 1993. **47**. P. 4532; https://doi.org/10.1103/PhysRevB.47.4532.
26. Mikhailov S.A. Plasma instability and amplification of electromagnetic waves in low-dimensional electron systems. *Phys. Rev. B*. 1998. **58**. P. 1517; Tunable solid-state far-infrared sources: New ideas and prospects. *Recent Res. Devel. Appl. Phys.* 1999. **2**. P. 65; https://doi.org/10.1103/PhysRevB.58.1517.
27. Korotyeyev V.V., Kochelap V.A., Danylyuk S., and Varani L. Spatial dispersion of the high- frequency conductivity of two-dimensional electron gas

subjected to a high electric field: collisionless case. *Appl. Phys. Lett.* 2018. **113**. P. 041102; https://doi.org/10.1063/1.5041322.
28. Mikhailov S.A., Savostianova N.A. and Moskalenko A.S. Negative dynamic conductivity of a current-driven array of graphene nanoribbons. *Phys. Rev. B.* 2016. **94**. P. 035439; https://doi.org/10.1103/PhysRevB.94.035439.
29. Koseki Y., Ryzhii V., Otsuji T., Popov V.V., and Satou A. Giant plasmon instability in a dual-grating-gate graphene field-effect transistor. *Phys. Rev. B.* 2016. **93**. P. 245408; https://doi.org/10.1103/PhysRevB.93.245408.
30. Petrov A.S., Svintsov D., Ryzhii V., Shur M.S. Amplified-reflection plasmon instabilities in grating-gate plasmonic crystals. *Phys. Rev. B.* 2017. **95**. P. 045405; https://doi.org/10.1103/PhysRevB.95.045405.
31. Kim K.W., Korotyeyev V.V., Kochelap V.A., Klimov A.A. and Woolard D.L. Tunable terahertz-frequency resonances and negative dynamic conductivity of two-dimensional electrons in group-III nitrides. *J. Appl. Phys.* 2004. **96**. P. 6488; https://doi.org/10.1063/1.1811388.
32. Lu J.T., Cao J.C. and Feng S.L. Hot-electron dynamics and terahertz generation in GaN quantum wells in the streaming transport regime. *Phys. Rev. B.* 2006. **73**. P. 195326; https://doi.org/10.1103/PhysRevB.73.195326.
33. Shiktorov P., Starikov E., Gruzinskis V., Varani L., Palermo C., Millithaler J-F. and Reggiani L. Frequency limits of terahertz radiation generated by optical-phonon transit-time resonance in quantum wells and heterolayers. *Phys. Rev. B.* 2007. **76**. P. 045333; https://doi.org/10.1103/PhysRevB.76.045333.
34. Korotyeyev V.V., Kochelap V.A., and Varani L. Wave excitations of drifting two-dimensional electron gas under strong inelastic scattering. *J. Appl. Phys.* 2012. **112**. P. 083721; https://doi.org/10.1063/1.4759277.
35. Laurent T., Sharma R., Torres J. et al. Voltage-controlled sub-terahertz radiation transmission through GaN quantum well structure. *Appl. Phys. Lett.* 2011. **99**. P. 082101; https://doi.org/10.1063/1.3627183.
36. Ambacher O., Foutz B., Smart J. et al. Two dimensional electron gases induced by spontaneous and piezoelectric polarization in undoped and doped AlGaN/GaN heterostructures. *J. Appl. Phys.* 2000. **87**. P. 334; https://doi.org/10.1063/1.371866.
37. Sydoruk V.A., Zadorozhnyi I., Hardtdegen H. et al. Electronic edge-state and space-charge phenomena in long GaN nanowires and nanoribbons. *Nanotechnology.* 2017. **28**. P. 135204; *Fluctuation and Noise Letters.* 2017. **16**. P. 1750010; https://doi.org/10.1088/1361-6528/aa5de3.
38. Sakai K. (Ed.): Terahertz Optoelectronics. *Topics Appl. Phys.* 2005. **97**. P. 1–31; https://doi.org/10.1007/b80319.
39. Matov O.R., Meshkov O.F., and Popov V.V. Spectrum of plasma oscillations in structures with a periodically inhomogeneous two-dimensional electron plasma. *Zh. Eksp. Teor. Fiz.* 1998. **113**. P. 988 [*JETP.* 1998. **86**. P. 538]; https://doi.org/10.1134/1.558500.
40. Ordal M.A., Long L.L., Bell R.J., Bell S.E., Bell R.R., Alexander R.W., Ward C.A. Optical properties of the metals Al, Co, Cu, Au, Fe, Pb, Ni, Pd, Pt, Ag, Ti, and W in the infrared and far infrared. *Appl. Optics.* 1983. **22**. P. 1099; https://doi.org/10.1364/AO.22.001099.
41. Levinstein M., Rumyantsev S., and Shur M. *Properties of Advanced Semiconductor Materials: GaN, AlN, InN, BN, SiC, SiGe*. Wiley, New York, 2001.
42. Rajab K.Z., Naftaly M., Linfield E.H., Nino J.C., Arenas D., Tanner D., Mittra R., and Lanagan M. Broadband dielectric characterization of aluminum oxide (Al_2O_3). *Micro and Elect. Pack.* 2008. **5**. P. 101–106; https://doi.org/10.4071/1551-4897-5.1.1.
43. Glasko V.B., Khudak Yu.I. Additive representations of the characteristics of plane-layered media and the uniqueness of the solution of converse problems. *USSR Computational Mathematics and Mathematical Physics.* 1980. **20**. P. 213–222; https://doi.org/10.1016/0041-5553(80)90035-X.

Authors and CV

Dr. Vadym Korotyeyev born 1977 in Lutsk (Volyn region, Ukraine), graduated in physics in 1999, the Ph.D. degree in solid state physics in 2006 from the V. Lashkaryov Institute of Semiconductor Physics, NAS of Ukraine. Since 2010, he is senior researcher at the Department of Theoretical Physics of the V. Lashkaryov Institute of Semiconductor Physics, NASU. He is author of more than 20 publications. His main research activity is in the field of electronic transport in nanoscaled structures and THz optoelectronics.

Dr. Yurii Lyaschuk born 1988 in Ostriv (Rivne region, Ukraine), graduated in physics in 2010 (Eastern European National University), the Ph.D. degree in semiconductor physics in 2018 from the V. Lashkaryov Institute of Semiconductor Physics, NAS of Ukraine. Since 2016, he is junior researcher at the Department of electrical and galvanomagnetic properties of semiconductors in Institute of Semiconductor Physics, NASU. He is author of 12 publications. His main research activity is in the field of electrodynamics of low-dimensional systems, THz plasmonics and optoelectronics.

Prof., Dr. Viatcheslav A. Kochelap born 1944 in Kyiv (Ukraine), graduated in theoretical physics in 1966 (Kiev State University), the Ph.D. degree in solid state physics in 1970 from Institute of Semiconductor Physics NAS of Ukraine. Since 1987, he is full Professor at the Department of Theoretical Physics at the V. Lashkaryov Institute of Semiconductor Physics, NASU. He is author of more than 250 publications. His main research activity is in the field of electronic transport, fluctuation phenomena and THz-physics of semiconductors and semiconductor nanoscale devices.

Prof. Luca Varani was born in Carpi, Italy, in 1963. He received the Ph.D. degree in physics from the University of Modena, Italy, in 1993, and the Ph.D. degree in electronics from the University of Montpellier, France, in 1996. His main research interest is in theoretical and experimental transport phenomena in semiconductor materials and devices with a special attention to the terahertz frequency range. He is author and coauthor of about 380 scientific articles in refereed journals and conference proceedings.

Dr. Dominique Coquillat received the PhD degree in semiconductor physics from the University of Montpellier. She is currently Director of Research at CNRS and University of Montpellier. Her current research interests include terahertz frequency optics and electronics, and non-destructive THz sensing for Agro-Environment. She has published over 200 publications in peer-reviewed research papers and 4 international patents.

Dr. rer. nat. Serhiy Danylyuk is a group leader for EUV Technology at the Chair for Technology of Optical Systems at RWTH Aachen University, Germany. He received his diploma in physics from Volyn State University, Ukraine, in 1999 and obtained his PhD in semiconductor physics from RWTH Aachen University, Germany. Since 2011 he is leading EUV Technology group working on applications of EUV radiation for nanopatterning, microscopy and thin film characterization. He is an author and co-author of more than 90 scientific publications in the fields of semiconductor physics and applications of short-wavelength radiation.

Dr. Sascha Brose born 1985 in Düren (Germany), graduated in mechanical engineering 2007 (University of Applied Science Aachen, Germany) and received the Ph.D. degree in mechanical engineering in 2019 from RWTH Aachen University, Germany. He is author of 17 publications. Since 2009 he is working in the field of applications for the extreme ultraviolet (EUV) at the RWTH Aachen University concentrating on the conceptual design and construction of EUV tools for high-precision metrology and nanoscale patterning.

Prof. Dr. Svetlana Vitusevich born 1959 in Kyiv (Ukraine), graduated in radiophysics and electronics in 1991 (Kiev State University), the Ph.D. degree in physics and mathematics in 1991 from ISP, NASU; the Dr. Sci. degree in 2006 from the Supreme Attestation Commission of Ukraine and Dr. Habil. degree in 2006 from Technical University of Dortmund, Germany. Since 2017, she is full Professor at ISP, NASU and at Forschungszentrum Juelich, Germany. She is author of more than 240 publications and 9 patents. Her research interests include transport and noise properties of novel device structures for future information technologies.